Journal of Marine Research, 58, 585–607, 2000

The cyclonic turning and propagation of buoyant coastal discharge along the shelf

by Alexander E. Yankovsky[1]

ABSTRACT

Buoyant coastal discharge typically forms a current flowing along the coast in the direction of Kelvin wave propagation (hereinafter referred to as the downstream direction). In this paper the opposite, upstream penetration of buoyancy-driven current is studied using numerical modeling. Previous models of coastal buoyancy-driven currents repeatedly predicted the upstream spreading while in the field this feature was not commonly observed. The mechanism responsible for the propagation of buoyant flow along the coast upstream from its source is identified as follows.

In many cases, the boundary conditions applied for buoyant discharge oversimplify the actual dynamics at the mouth blocking landward flow in the lower layer. This generates a strong cyclonic vorticity disturbance with corresponding upstream turning of buoyant flow at the source. This process initiates the upstream spreading of buoyant flow. Alternative boundary condition maintaining constant net transport but allowing baroclinic adjustment of buoyant inflow is formulated and shown to reduce the generation of cyclonic vorticity at the mouth.

The upstream propagation is further enhanced by the vertical mixing. The buoyant water forms an anticyclonic bulge at the river or estuary mouth. While spreading around the center of this anticyclone, the fresher water gradually becomes saltier due to vertical mixing/diffusion. As a result, the pool of lightest water does not coincide with the center of the anticyclone (in the sense of integral streamfunction) but tends to occupy the upstream and inshore segment of the bulge where the buoyant water comes first. This sets a new center for the anticyclonic turning at the surface and promotes the upstream shift of the anticyclonic bulge. This process sustains continuous growth of the buoyant plume upstream. It is shown that the upstream ambient current does not produce a similar effect. Instead, buoyant flow periodically sheds anticyclones advected upstream with the mean current. Under certain conditions, upstream spreading is also possible in nature. For example, Beardsley *et al.* (1985) reported substantial upstream penetration of the Changjiang River discharge in the East China Sea during the period of high runoff.

1. Introduction

There is persistent interest in the dynamics of buoyant coastal plumes associated with fresh water discharge on the continental shelf. These buoyant plumes are subjects of both observational and numerical modeling studies. The buoyancy-driven currents typically propagate along the coast in the downstream direction (i.e., in the direction of Kelvin wave

1. Nova Southeastern University, Oceanographic Center, 8000 North Ocean Drive, Dania Beach, Florida, 33004-3078, U.S.A. ***email: sasha@nova.edu***

propagation) which is readily explained by their semi-geostrophic nature. This propagation has been repeatedly observed in the field and also simulated in models. However, numerical experiments also reveal upstream spreading of the buoyant discharge. In many cases, the buoyant inflow first turns to the left (facing offshore at the mouth in the northern hemisphere) upon entering the shelf and only thereafter executes anticyclonic turning and forms a downstream flow. The buoyant plume keeps advancing upstream, albeit at a lower speed than the downstream propagation. This pattern was present in the model studies by Chao and Boicourt (1986), Chapman and Lentz (1994), Kourafalou *et al.* (1996), Fong (1998), Garvine (1999), etc. The upstream spreading appears to be a robust feature in primitive equation numerical models but this behavior is rarely observed in the coastal ocean. One of few observational examples is the substantial upstream penetration of the Changjiang River discharge in the East China Sea reported by Beardsley *et al.* (1985).

Why do the models repeatedly predict upstream spreading while in the field this feature is not commonly observed? Is this upstream spreading essentially an artifact of numerical calculations? What is the mechanism sustaining continuous upstream propagation? This study means to address these questions.

There were several attempts to explain this effect in the previous studies. Chapman and Lentz (1994) described the upstream flow in terms of momentum and heat balances. They pointed out the importance of the initial geostrophic adjustment of buoyant inflow that generated an upstream current near the coastal wall. This set an upstream buoyancy flux which maintained the continuous upstream propagation. McCreary *et al.* (1997) focused on the upstream spreading of buoyant discharge in their study. They treated this problem using a hierarchy of variable-density 1.5 layer models (both analytical and numerical). They found that mixing of the discharged and ambient water formed a frontal zone with the downstream buoyancy-driven flow. The net downstream transport by this frontal current drained the ambient water at the source region. The upstream spreading of the buoyant plume resulted in compensation for this loss of mass.

Apart from the importance of mixing, the vorticity balance of the discharged flow has been argued to be significant for the near-source adjustment. Woods and Beardsley (1988) analyzed the adjustment of barotropic discharge on a sloping frictional shelf. They found that for low discharge velocity, the flow turned to the right and evolved in the manner of the arrested topographic wave (ATW) solution of Csanady (1978), i.e., the flow was controlled by bottom friction. When the discharge velocity increased, advection became more important and cyclonic vorticity was induced by the topographic stretching of the inflow. This cyclonic vorticity caused the inflow deviation to the left at the source with a subsequent anticyclonic turn to the right and downstream propagation. The initial left turning, however, did not lead to continuous upstream propagation, as in the cases of buoyant discharge. Kubokawa (1991) investigated the evolution of the inflow with low potential vorticity (LPV) into the coastal ocean. He showed that the downstream coastal current had a limited capacity to transport LPV fluid and the excessive LPV inflow could

cause the offshore and upstream expansion of the coastal current near the source of discharge.

We offer a different explanation for the buoyant upstream spreading, even though both relative vorticity generation and mixing are found to be important. Section 2 describes the model and the design of numerical experiments. In Section 3, we present model results which elucidate the cyclonic excursion of buoyant inflow and (separately) the continuous spreading of buoyant flow upstream. The emphasis is made on surface-advected plumes (when the buoyant layer overlays the ambient water—for details see Yankovsky and Chapman [1997], hereinafter referred to as YC97). Bottom-advected plumes (when the buoyant flow is in contact with a frictional bottom) are mentioned only briefly since they seem to be less common features. Section 4 discusses the relevance of our results to other modeling studies and also to available observations. Section 5 concludes and summarizes this study.

2. Model formulation

We utilize the primitive equation model (SPEM) developed by Haidvogel *et al.* (1991), the 5.1 version. The following momentum and mass balance equations describe the evolution of fluid under the Boussinesq, *f*-plane and hydrostatic approximations:

$$u_t + \mathbf{v} \cdot \nabla u - fv = -\frac{1}{\rho_0} p_x + A_H \nabla_\sigma^2 u + (A_v u_z)_z \tag{2.1}$$

$$v_t + \mathbf{v} \cdot \nabla v + fu = -\frac{1}{\rho_0} p_y + A_H \nabla_\sigma^2 v + (A_v v_z)_z \tag{2.2}$$

$$p_z = -g\rho \tag{2.3}$$

$$u_x + v_y + w_z = 0 \tag{2.4}$$

$$\rho_t + \mathbf{v} \cdot \nabla \rho = K_H \nabla_\sigma^2 \rho + (K_v \rho_z)_z. \tag{2.5}$$

Here $\mathbf{v}$ is the velocity vector with u, v, w components along the x, y, z coordinates; ρ is the density difference from a reference (constant) density of the ambient flow $\rho_0 = 1020$ kg m^{-3}; p is the pressure; $f = 10^{-4}$ s^{-1} is the Coriolis parameter and g is the acceleration due to gravity. The subscripts t, x, y, z denote partial differentiation with respect to time and spatial coordinates. The coefficients for vertical eddy viscosity A_v and diffusivity K_v are parameterized using the Mellor-Yamada 2.0 closure scheme (Mellor and Yamada, 1974), unless otherwise noted. Lateral Laplacian mixing and diffusion are applied along the σ-coordinate surfaces with constant coefficients A_H and K_H, respectively.

The model domain is a channel bounded by two parallel vertical walls (Fig. 1, upper panel). The shallower coastal wall of depth $h_0 = 15$ m coincides with the x-coordinate while the y-coordinate points offshore. The depth h increases linearly in the y direction with bottom slope $s = 0.002$. The channel's width is 80 km. The across-channel boundaries are

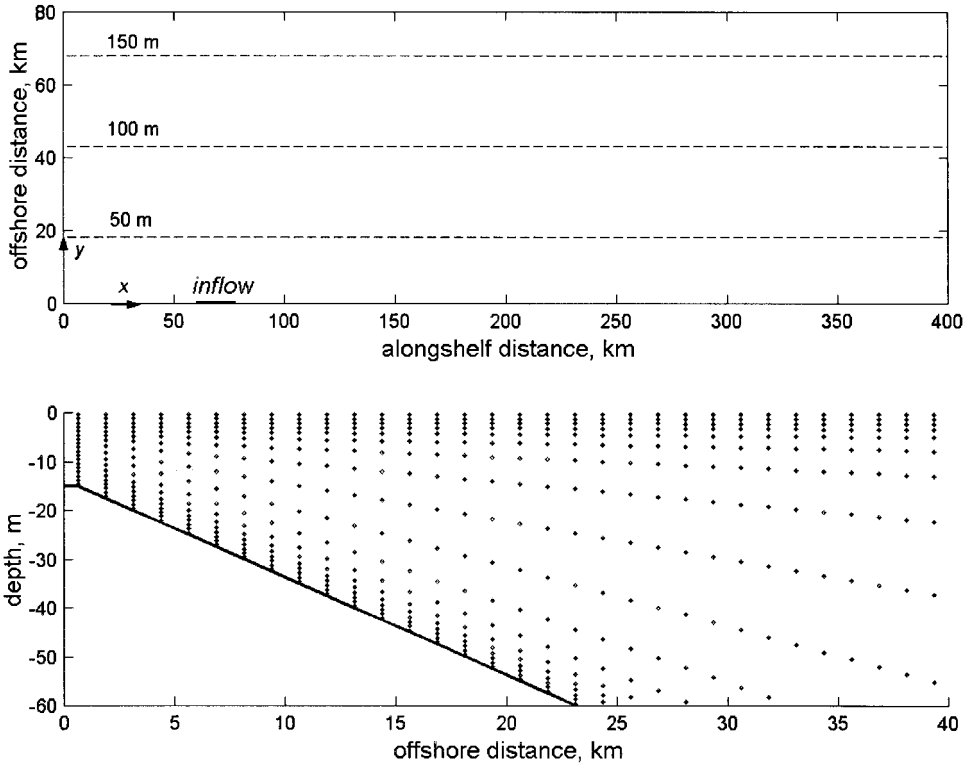

Figure 1. Model geometry: plan view of the model domain (upper panel) and offshore transect showing the vertical grid spacing (lower panel). Heavy line is bottom.

at $x = 0$ and 400 km with the open boundary conditions discussed below. The numerical grid is rectangular in the horizontal with uniform grid spacing in both coordinates: $\Delta_x = 2.5$ km (161 grid cells in x) and $\Delta_y = 1.25$ km (65 grid cells in y). The conventional sigma-coordinate grid in SPEM5 is generalized to retain high vertical resolution in the dynamically important surface and bottom layers, while a stretched (topography following) coordinate is applied in the interior. We use 18 grid cells in the vertical (Fig. 1 lower panel) with their numeration from the bottom (1) to the surface (18). The enhanced resolution of near-surface and near-bottom layers allows us to resolve the dynamics of surface-advected and bottom-advected plumes, respectively. The model time step is 240 s.

The following boundary conditions are applied. A rigid lid is assumed at the surface. There is no normal flow through the bottom and walls except for the buoyant discharge through the coastal wall which forces the model. A buoyant inflow is specified through the gap with the upstream edge located at $x = 60$ km and typical width set to $L = 17.5$ km. The inflow has uniform velocity v_i and density anomaly ρ_i. The walls are slippery (no stress), while the bottom is frictional and the stress is specified using a linear bottom friction

parameterization,

$$A_v u_z = ru; \qquad A_v v_z = rv; \qquad z = -h, \tag{2.6}$$

where $r = 2.65\ 10^{-4}$ m s^{-1} is the bottom friction coefficient. The background (minimum) values of the vertical viscosity and diffusivity coefficients in the Mellor-Yamada closure scheme are set to be $2\ 10^{-5}$ m^2 s^{-1}. The coefficients of lateral mixing and diffusion are constant: $A_H = K_H = 20$ m^2 s^{-1}.

Since the discharge propagates downstream (in the positive x direction), we apply the radiation boundary condition for depth-averaged velocity components (YC97, Chapman and Lentz, 1994). This radiation condition is based on the assumption that vorticity associated with the depth-averaged velocity propagates through the open boundary at a constant speed. A "smooth" condition (zero x-derivative) is applied to the depth-varying quantities at both up- and downstream open boundaries.

Initially, the water in the domain is quiescent and of constant density anomaly $\rho = 0$. The buoyant inflow is imposed and is held constant through the model run. The model run's duration is 30 days. This time is long enough for the development of significant upstream spreading in those cases when the model set up promotes this process.

3. Results

a. Cyclonic turning of buoyant discharge

In this subsection we will present the consecutive set of model runs which demonstrate that the cyclonic (i.e., upstream) turning of a buoyant current at the source results from the baroclinic adjustment of the discharged buoyant flow. This cyclonic turning is also affected (amplified) by the depth- and time-independent boundary conditions imposed for buoyant discharge. However, this subsection does not deal specifically with the enhanced upstream propagation that we referred to in the Introduction.

As a starting point, we consider barotropic inflow, $\rho_i = 0$, (model run 1). The flow is discharged through a gap in the coastal wall of width $L = 17.5$ km with an inflow velocity $v_i = 0.1$ m s^{-1}. The Rossby number of the inflow is $Ro = v_i/fL = 0.057$. This is a rather low value and so advection is not significant. Figure 2 shows the integral streamfunction and surface velocity on day 30, when the flow has achieved a steady-state regime. The inflow immediately turns to the right and after that it gradually expands offshore while propagating downstream. The offshore "diffusion" of the streamfunction and velocity fields is a result of bottom friction. This behavior is in agreement with the ATW solution and also with the low-inflow regime described by Woods and Beardsley (1988).

A remarkably different regime occurs when the same inflow has a finite density anomaly. In the next model run (run 2), we specify $\rho_i = -2.5$ kg m^{-3}. This discharge produces a surface-advected plume (YC97) in which case the buoyant layer spreads over the ambient water and the bottom Ekman layer does not deepen the buoyant flow. We define the baroclinic Rossby radius of the buoyant inflow as $R_{di} = (g' h_0)^{1/2}/f$ where $g' = g|\rho_i|/\rho_0$ is reduced gravity. For the model run 2, $R_{di} = 6$ km while the Burger number is $S = R_{di}/L =$

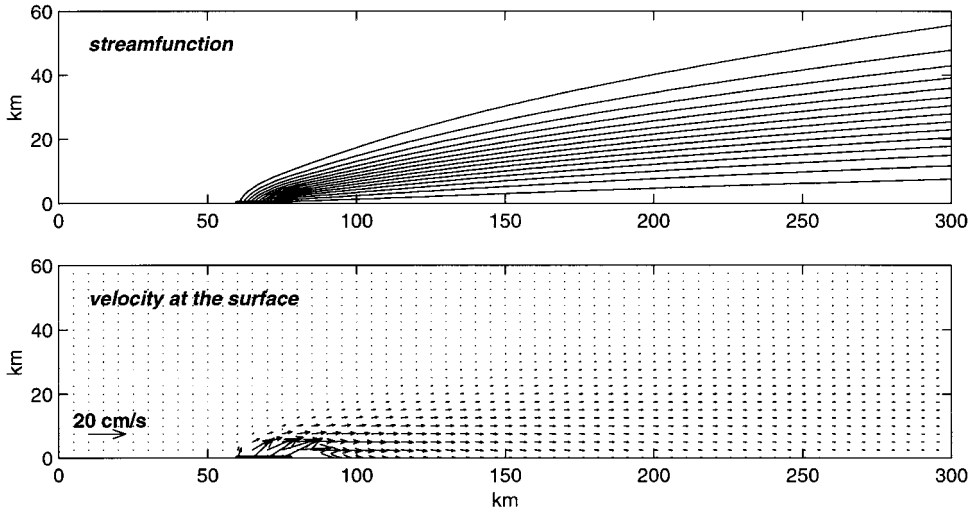

Figure 2. Model run 1, day 30. Plan views of streamfunction (upper panel) and velocity at the surface (lower panel).

0.34. When $S < 1$, the effect of rotation is important for the buoyant discharge dynamics (Garvine, 1995).

Figure 3 shows the streamfunction, density anomaly at the surface and velocity at the surface on day 20. The buoyant inflow forms an anticyclonic bulge near its source and then continues downstream as a narrower coastal current trapped against the wall. All these features are well known from previous studies. An interesting point is that the inflow deviates to the left (upstream) as it enters the domain and only after that turns anticyclonically. This pattern exhibits itself not only at the surface (i.e., density and velocity at the surface) but in the integral streamfunction field as well. Still there is no predominantly upstream spreading of the buoyant discharge. Instead, the bulge keeps growing and spreads laterally from its source in all directions. This is clearly seen in Figure 4 which shows the temporal evolution of the density anomaly contour -1.25 kg m^3. This contour represents the center of the frontal zone separating plume from the ambient water.

The cyclonic turn of the inflow cannot be explained by the topographic stretching of the buoyant layer since it does not deepen while spreading offshore, consistent with the surface-advected plume regime. Instead, we will identify a different cause for this cyclonic turning. Figure 5 shows the streamfunction and the relative vorticity associated with it at the earlier stage of the plume's formation for the model runs 1 and 2, both on day 5. The major difference in vorticity distribution between the two cases occurs at the upstream edge of the inflow ($x = 60$ km). For the barotropic discharge (run 1), there are two comparable disturbances in the relative vorticity at the edges of the inflow: a cyclonic disturbance at the upstream edge ($x = 60$ km) and an anticyclonic one at the downstream edge ($x = 78$ km). These two features are caused by the discontinuities in the offshore component of velocity

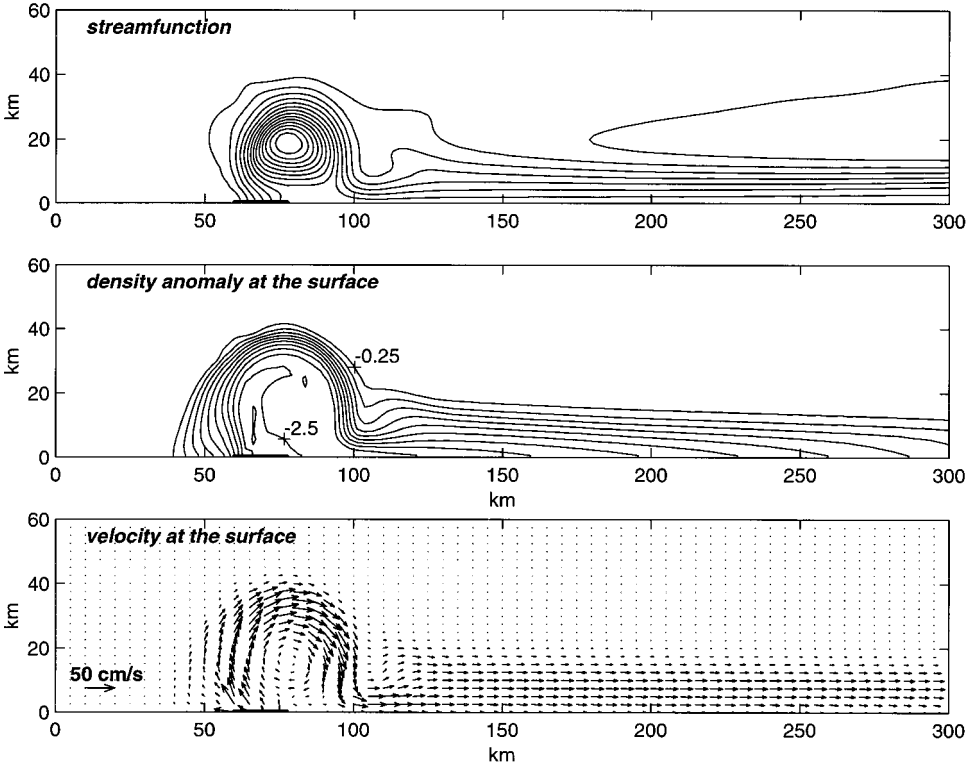

Figure 3. Model run 2, day 20. Plan views of streamfunction (top panel), density anomaly at the surface with the contour interval at 0.25 kg m^3 (middle panel), and velocity at the surface (bottom panel).

at the edges of the source. Model run 2, representing the buoyant discharge, has strong and spatially localized cyclonic vorticity at the upstream edge of the inflow where the streamlines turn cyclonically (upstream). This cyclonic disturbance greatly exceeds its anticyclonic counterpart at the downstream edge of the inflow.

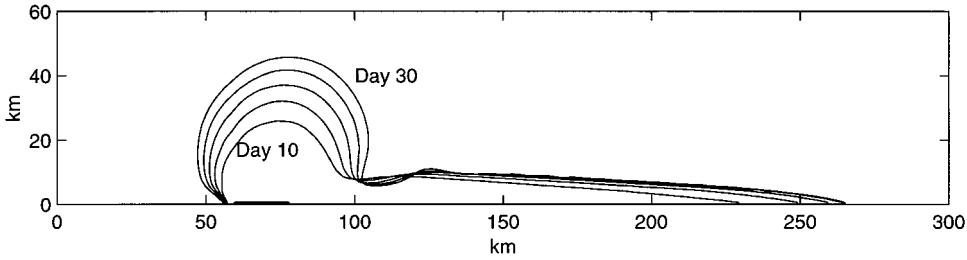

Figure 4. Model run 2, location of density anomaly contour −1.25 kg m^3 at the surface shown at 5-day intervals from day 10 through day 30.

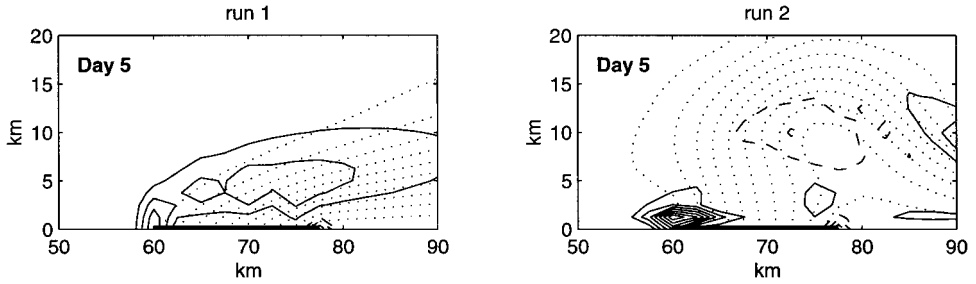

Figure 5. Relative vorticity of the vertically integrated flow at the inflow region on day 5 of model run 1 (left panel) and 2 (right panel). Solid (dashed) contours represent positive (negative) vorticity values at the interval 10^{-5} s^{-1}, zero contour is not shown. Dotted lines are streamfunction contours.

In the case of buoyant discharge, the baroclinic adjustment of the inflow generates vertical shear of velocity in the model interior. Indeed, Figure 6 (solid line) shows that the offshore velocity component v changes from almost 0.4 m s^{-1} at the surface to -0.1 m s^{-1} near the bottom at the grid point next to the coastal boundary where the inflow is specified. The offshore velocity has better pronounced vertical structure at the upstream edge of the discharge ($x = 61.25$ km, solid line in Fig. 6) than at the middle ($x = 66.25$ km, dashed line) or at the downstream edge (not shown). This is because the upstream edge of the discharged flow represents a frontal zone separating buoyant and ambient water. The strong horizontal density gradient across the frontal zone sets the vertical geostrophic shear. On the other hand, the buoyant discharge at the boundary remains vertically uniform (dotted line in Fig. 6). Thus, it is natural to suggest that the transition from the depth-independent structure of the inflow to the baroclinic regime in the interior induces this strong cyclonic vorticity feature.

Now we consider the vertical component of vorticity $v_x - u_y$ at particular σ-levels. Figure 7 (left) shows the vertical distribution of vorticity in the center of cyclonic disturbance. This profile is at the same location as the v-component in Figure 6 (solid line), i.e., near the upstream edge of the inflow and one gridpoint offshore from the boundary. The maximum cyclonic vorticity disturbance occurs through the lower half of the water column while at the surface the vorticity is anticyclonic (negative). The horizontal divergence term $u_x + v_y$ (Fig. 7 right) indicates significant convergence near the bottom in the layer 10–16 m deep. This convergence is clearly related to both bottom stress and strong vertical shear of vorticity near the bottom, i.e., it has a frictional nature. This convergence in the lower layer is compensated by divergence in the surface layer with resulting upstream excursion of buoyant inflow.

In order to further understand the generation of cyclonic vorticity, we consider the velocity and density (Fig. 8) distribution on two sigma surfaces: level 6 (crossing the coastal wall at 10 m depth) and level 18 (surface). These two sigma levels represent lower and upper dynamical layers, respectively, near the coast. Surface current concentrates

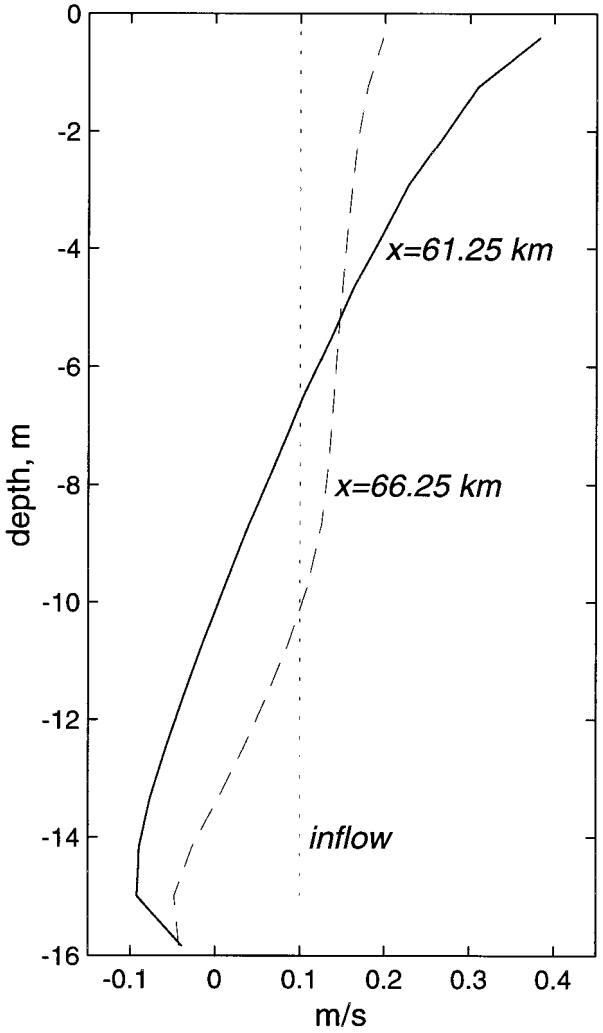

Figure 6. Model run 2, day 5. Vertical profiles of the velocity component, v, 1.25 km offshore at $x =$ 61.25 km (solid line), $x = 66.25$ km (dashed line). Dotted line is the inflow velocity at the boundary ($60 < x < 77.5$ km, $y = 0$ km).

within the frontal zone that separates ambient water from the expanding buoyant bulge. Both velocity and density fields at the surface approximately correspond to the streamfunction pattern (compare Fig. 8, left with Fig. 5, right). However, there is no cyclonic vorticity feature at the upstream edge of the buoyancy source near the surface (Fig. 7). Instead, the cyclonic vorticity concentrates in the lower layer. Current at level 6 opposes the surface current and also the net transport of buoyant flow (i.e., streamfunction). This is a consequence of vertical shear due to the presence of a strong density anomaly (thermal

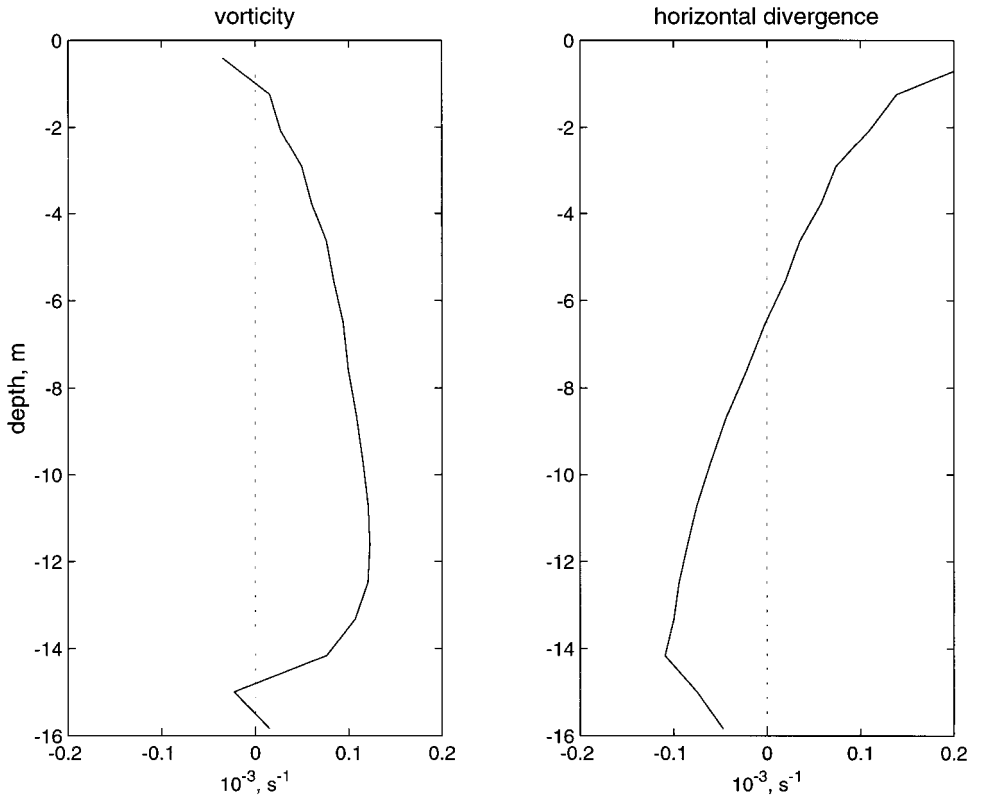

Figure 7. Model run 2, day 5. Vertical profiles of the vorticity ($v_x - u_y$) (left panel) and horizontal divergence ($u_x + v_y$) (right panel) at $x = 61.25$ km, $y = 1.25$ km.

wind balance). This countercurrent in the lower layer flows along the outer part of the frontal zone which is near the coast at this depth, corresponding to the surface advected plume structure. The countercurrent collides with the "mouth" at the upstream edge of the buoyancy source where it is blocked by the superimposed inflow through the boundary

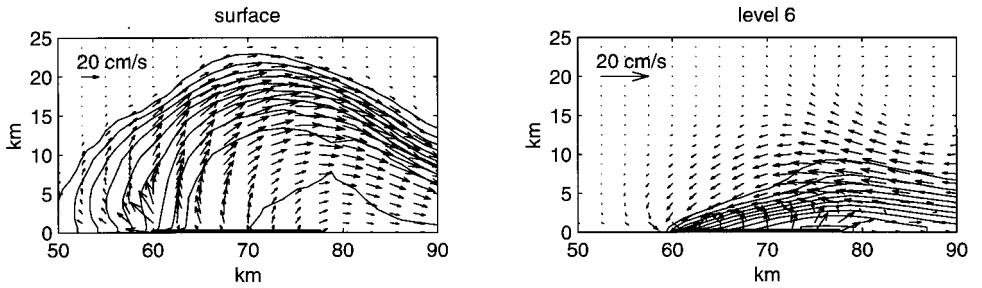

Figure 8. Model run 2, day 5, plan views of the velocity vectors and density anomaly (contour interval is 0.25 kg m^3) on the surface (left panel) and on the σ-level 6 (right panel).

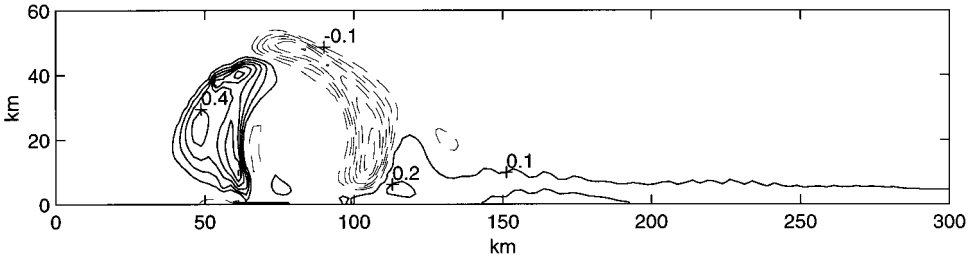

Figure 9. Plan view of the density anomaly difference between model run 3 and 2 at the surface, day 30 (values of run 2 are subtracted from run 3). Solid (dashed) contours are positive (negative) values at 0.1 kg m^3 interval while zero contour is not shown.

(Fig. 8). As a result of the interaction of the fixed inflow boundary condition and the onshore baroclinic flow near the bottom, a strong cyclonic feature forms, clearly visible in the velocity field at $x = 60$–62 km near the coast in Figure 8, right panel.

Thus, the adjustment of buoyant discharge generates baroclinic dynamics associated with the surface advected plume. A countercurrent in the lower layer is blocked by the imposed inflow boundary condition generating a strong cyclonic vorticity feature at the upstream edge of the inflow source. Interestingly, while the vorticity disturbance occurs in the lower layer, the upstream excursion of the buoyant flow takes place in the upper layer. This is achieved through the convergence near the bottom with compensating divergence at the surface.

The upstream excursion of buoyant inflow at the source is reduced when the inflow Rossby number is increased (while both net transport and the density anomaly are kept the same). The next model run (run 3) illustrates this tendency. Here all parameters are the same as in run 2, except the inflow enters the model domain through the narrower gap (10 km wide) at higher velocity ($v_i = 0.175$ m s^{-1}). The upstream edge of the gap is at the same x-coordinate as in the previous run. The inflow Rossby number ($Ro = 0.175$) is tripled compared to the previous case. The resulting model fields look rather similar to model run 2, so we plot the difference between runs 3 and 2 (values of run 2 are subtracted from run 3). The density anomaly difference at the surface on day 30 is presented in Figure 9, where the negative values denote relatively lighter water in model run 3 while the positive values represent heavier water compared to run 2. Figure 9 shows that heavier water occupies the upstream part of the bulge while lighter water is at the downstream part. As a whole, the buoyant bulge is bent downstream compared to model run 2.

These model runs identified our boundary condition for buoyant discharge (i.e., fixed in time and depth-independent) as the cause for the strong cyclonic vorticity disturbance with a resulting upstream excursion of the buoyant inflow. In the next numerical experiment (model run 4) we introduce a different boundary condition for v at the mouth that allows feedback of the interior dynamics to the vertical structure of the inflow. This baroclinically adjusted boundary condition is designed to reduce the blockage of the near-bottom counter-current through the mouth. On the other hand, the horizontal structure of the

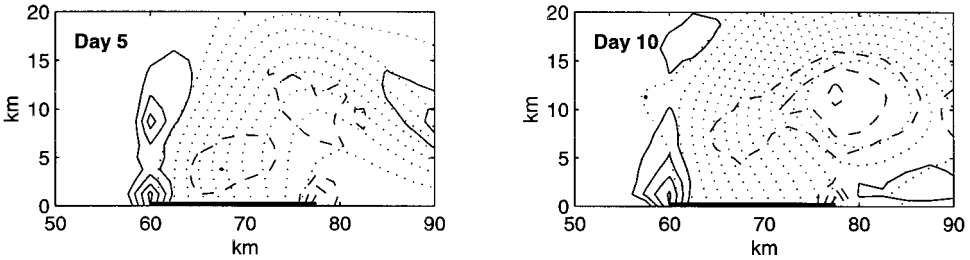

Figure 10. As in Figure 5 but for the model run 4, day 5 (left panel) and day 10 (right panel).

vertically integrated inflow remains the same as in previous model runs. Now we define the depth-dependent v component through the coastal gap ($60 < x < 77.5$ km) at $y = 0$ as follows:

$$v(x, 0, \sigma) = C(x)v(x, \Delta_y, \sigma)$$
$$C(x) = h_0 v_i \Big/ \int_{-h}^{0} v(x, \Delta_y, z)\, dz \tag{3.1}$$

where v_i is the depth-independent inflow velocity specified in the previous model runs. Thus, the vertical profile of the v component at every grid cell across the mouth is similar to its neighbor in the interior (if introduced in σ-coordinate). However, the $C(x)$ coefficient provides constant in time vertically integrated transport of the buoyant water into the domain which is the same as in model run 2 for every horizontal grid cell. During the 1st hr of model computations, the inflow velocity is depth-independent (as in previous runs); after that the (3.1) condition is applied. We also linearly increase ρ_i from 0 to -2.5 kg/m^3 (maximum value) over a two-day period.

Model run 4 demonstrates the performance of this new boundary condition (Fig. 10). On day 5, the streamlines originating from the mouth do not deviate to the left (facing offshore). Instead, they continue straight into the domain and gradually turn to the right (anticyclonically). Accordingly, the cyclonic vorticity feature at the upstream edge of the inflow is much weaker than in model run 2 (Fig. 5) and is almost symmetric with the anticyclonic feature at the downstream edge. Later in time (day 10), streamlines start tilting slightly upstream, the result of continuously growing buoyant anticyclone. Still there is no enhanced cyclonic vorticity at the upstream edge of the discharge.

Plumes in model run 2 and 4 are driven by the same net transport of buoyant water entering the domain through a coastal gap of the same width. However, caution should be taken while comparing these two plumes. Indeed, discharge in model run 4 has vertical structure and is surface intensified with some reversal of flow near the bottom. Thus, the effective Ro and S for model run 4 differ from those for model run 2. The surface area of the anticyclonic bulge in model run 4 is greater compared to model run 2 while downstream penetration of the coastal buoyant current is shorter (Fig. 11). However, the most interesting feature from the perspective of this paper is that the bulge grows predominantly

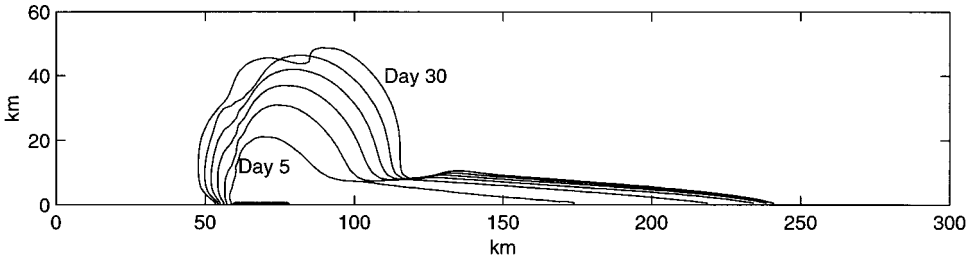

Figure 11. As in Figure 4 but for the model run 4, day 5 through day 30.

downstream from the source, in striking contrast with the almost radial growth in model run 2 (Fig. 4). The dynamics of the bulge in model run 4 is more nonlinear compared to the previous cases with some wiggle-like features both in density and velocity fields. This is likely a result of higher inflow velocity and stronger density gradient across the front (not shown). We conclude that the boundary condition (3.1) provides much smoother inflow of buoyant water into the domain and reduces the tendency of upstream excursion, especially at the earlier stages of plume development.

In the next subsection we will demonstrate how the initial upstream excursion of buoyant discharge can be translated into continuous upstream spreading of buoyant water along the coastal wall due to vertical mixing.

b. Upstream propagation of a buoyant plume

In the previous examples, the anticyclonic bulge grew and spread radially while the center of anticyclonic circulation remained stationary near the source of discharge. In this subsection we will consider a different regime of the buoyant plume, when the bulge continuously propagates upstream.

In the next numerical experiment (model run 5), we introduce constant vertical viscosity and diffusivity coefficients, both 10^{-4} m^2 s^{-1}. Otherwise the model configuration is the same as in model run 2. The increase of vertical mixing across the pycnocline triggers predominantly upstream spreading of the buoyant plume. By day 30 the plume has advanced upstream almost up to the model boundary (Fig. 12). The anticyclonic bulge develops upstream from the buoyancy source; the density anomaly at the surface within the bulge gradually changes from -2.5 kg m^{-3} at the source to less than -1.5 kg m^{-3} in the center of the anticyclone.

In order to emphasize the importance of density diffusion, we conducted two additional model runs with constant viscosity and diffusivity coefficients: in one case, the vertical viscosity is the same as the background level in the Mellor-Yamada scheme, that is 2 10^{-5} m^2 s^{-1}, while the diffusivity is 10^{-4} m^2 s^{-1} (run 6); in the other case the viscosity is 10^{-4} m^2 s^{-1} while the diffusivity is at the background level of the turbulence model (run 7). The temporal evolution of -0.25 kg m^3 density contour (representing 10% of the maximum density anomaly associated with the inflow) for both model runs is shown in

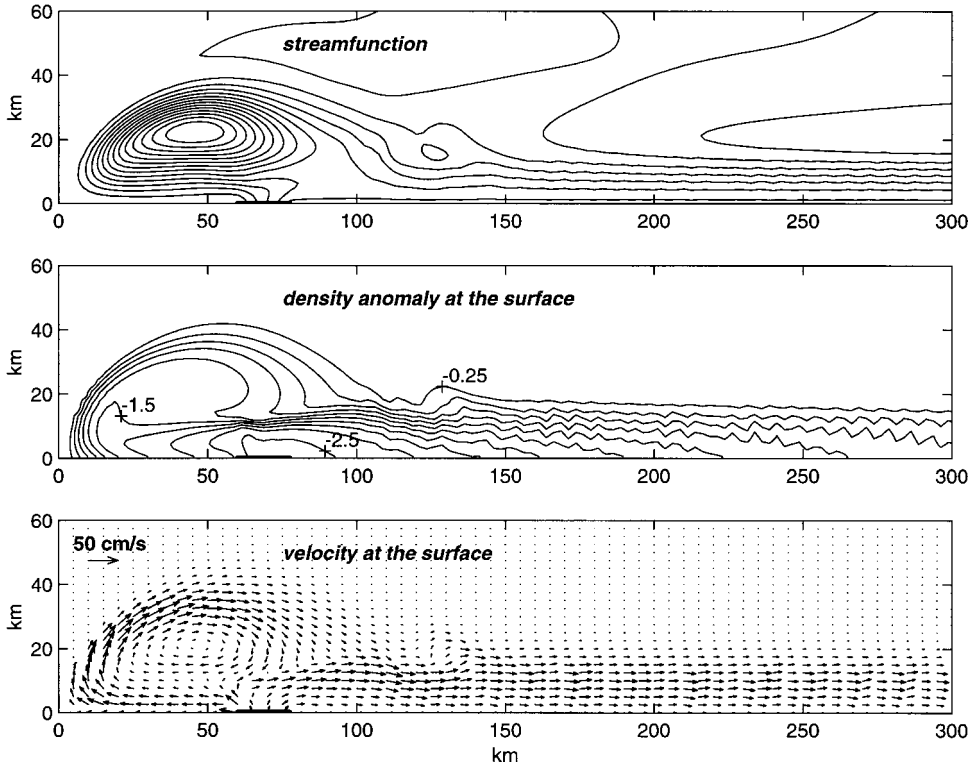

Figure 12. As in Figure 3 but for the model run 5, day 30.

Figure 13. In model run 6, the upstream propagation is even faster than it has been in run 5. On the other hand, there is virtually no upstream propagation in model run 7. Instead, buoyancy spreads symmetrically in all directions from its source, similar to the evolution in model run 2. The viscosity in the (seaward) shallowing pycnocline can induce upstream flow in the surface layer (Beardsley and Hart, 1978), but we have not found strong evidence for this mechanism in model run 7. Thus we conclude that vertical density mixing is responsible for the continuous spreading of buoyant discharge upstream compared to model run 2.

Figure 14 elucidates the nature of this upstream spreading. It shows the surface density distribution within the anticyclonic bulge relative to the integral streamfunction for two model runs, 2 and 5. Only density contours representing a density anomaly close to the inflow are plotted ($-2.5 \leq \rho \leq -2.0$ kg m^3). On day 10, upstream spreading is just starting to develop in model run 5, so the plumes in both cases look similar (upper panels). However, there is an important difference in the density field between the two plumes which ultimately leads to the different dynamics. The center of the anticyclonic flow (in the sense of streamline pattern) in model run 2 is filled with the almost uniform water of the same density as the buoyant discharge. On the other hand, the pool of lightest water in model run 5 occupies the upstream and inshore segment of the anticyclone and does not

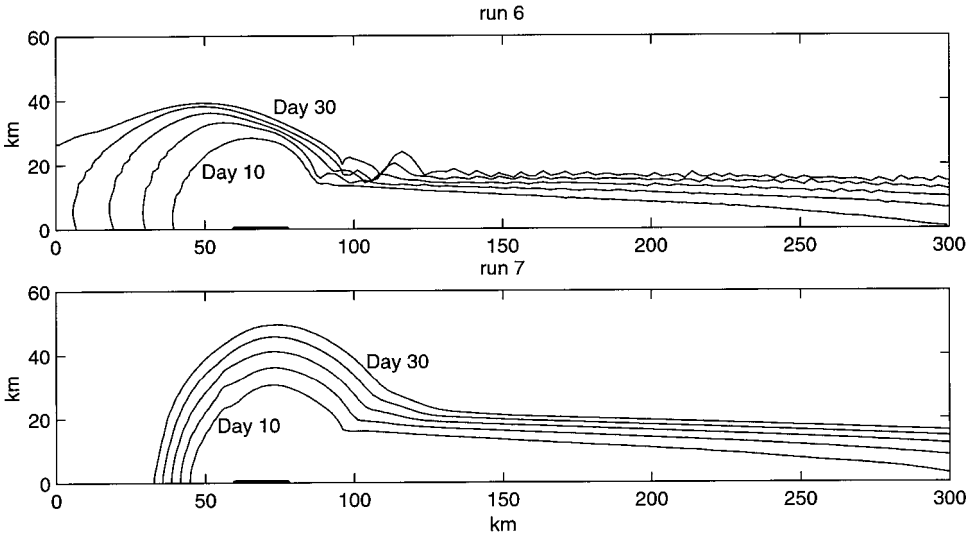

Figure 13. As in Figure 4 but for the density anomaly contour −0.25 kg m^3 in model run 6 (upper panel) and 7 (lower panel).

coincide with the center of anticyclonic circulation. This segment is part of the anticyclone where inflow arrives first. While the light water continues to flow around, it remains subject to enhanced vertical mixing. As a result, the surface density gradually increases from its initial value as the water flows farther away from its source around the bulge. Thus, when

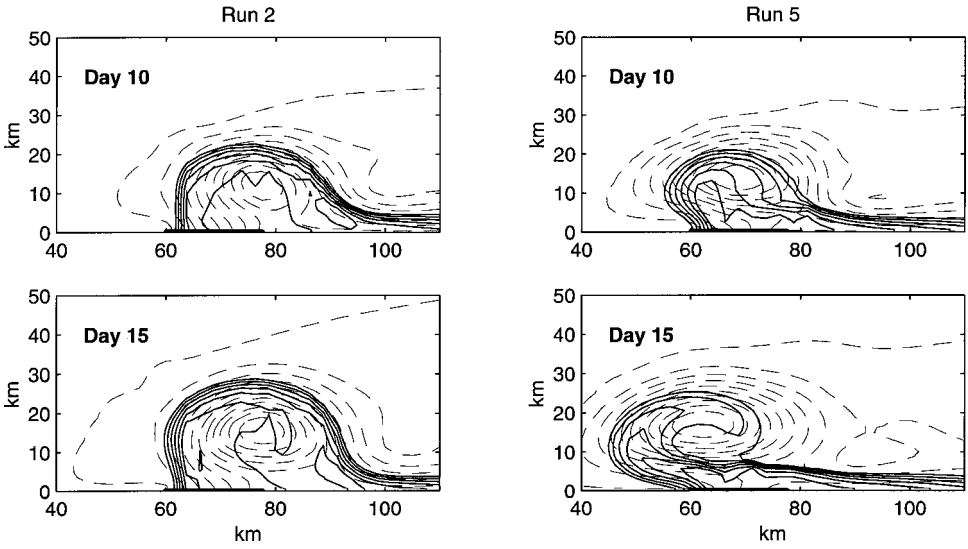

Figure 14. Plan views of density anomaly at the surface (solid contours are −2.5 to −2 by 0.1 kg m^3) and streamfunction (dashed contours) near the buoyancy inflow on day 10 (upper panels) and day 15 (lower panels) for model run 2 (left) and 5 (right).

the buoyant bulge has grown enough, vertical mixing prevents the lightest water from filling the center of anticyclonic circulation. Instead, the pool of lightest water shifts upstream and sets a new center for the anticyclonic flow at the surface while the streamlines follow this new pattern in surface circulation sustaining continuous upstream spreading.

Even weak alongshelf current flowing downstream can arrest the upstream propagation of buoyant discharge (YC97). Now we address the opposite question: can weak upstream current cause the upstream propagation of the plume similar to what we observed in the model run 5? In the next model run (run 8), we introduce a stationary, uniform upstream current of -0.05 m s^{-1} at the initial moment. We also apply an exponential depth profile which provides higher downstream propagation speed for transient features through the shelf wave mechanism:

$$h = h_0 e^{\lambda y} \tag{3.2}$$

where h_0 is again 15 m and λ is 6 10^{-5} m^{-1}. Finally, we place the source of buoyant inflow farther downstream ($185 < x < 202.5$ km). Otherwise the model configuration is the same as in model run 2.

The surface salinity fields on days 20, 30 and 40 are shown in Figure 15. The regime is quite different from run 5. Instead of forming an elongated anticyclone growing upstream (Fig. 12), the buoyant flow periodically sheds anticyclones from the source region. At the moment of separation from the source, the anticyclones have almost circular shape. After separation they continue to drift upstream, gradually mixing with the ambient flow. Yankovsky and Chapman (1997) derived a spatial scale *Ys* for the bulge of a stationary surface-advected plume:

$$Ys = 2(3g'h_0 + v_i^2)/f(2g'h_0 + v_i^2)^{1/2}. \tag{3.3}$$

They assumed that a steady-state regime could be achieved (for instance, in the presence of mean downstream current) and found good agreement between this scale and their model results. For our model parameters, $Ys = 25.5$ km. This scale is plotted as a vertical bar on the bottom panel (Fig. 15) and gives a good estimation for the eddy's size at the moment of its separation in the case of upstream flow as well.

The subsequent upstream propagating anticyclones generated by the source of buoyant inflow are qualitatively reminiscent of the results by Pichevin and Nof (1997). In their case, the separation and subsequent westward (upstream in our notation) drift was caused by the β-effect while in our case it is simply advection by the mean current.

c. Upstream propagation of a bottom-advected plume

In all previous numerical experiments we considered surface-advected plumes which spread over the ambient water and produced vertically stratified flow. A contrasting type of buoyancy-driven current is a bottom-advected plume when buoyant flow is in contact with the frictional bottom, spreading offshore due to the bottom Ekman transport. The plume

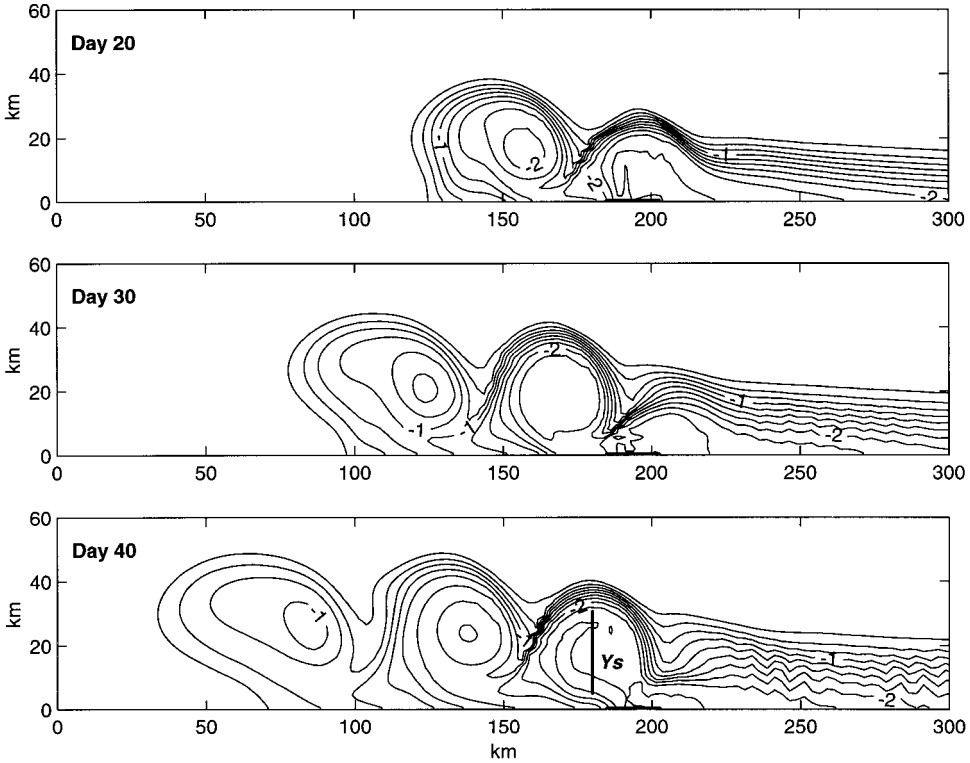

Figure 15. Model run 8, plan views of the density anomaly at the surface on day 20 (upper panel), day 30 (middle panel) and day 40 (bottom panel) with the contour interval at 0.25 kg m^3.

deepens as it spreads offshore and the frontal zone separates the buoyant water inshore and ambient water offshore. Chapman and Lentz (1994) described the physics of this type of plume while YC97 discussed how the properties of the buoyant discharge determined this type of plume. Typically, bottom-advected plumes are produced by inflow of low density anomaly and high volume transport. In this subsection, we will demonstrate that the upstream propagation of a bottom-advected plume develops in a similar manner to a surface-advected plume, even though these two types of plumes have different dynamics downstream from the source.

In the next numerical experiment (model run 9) we specify the inflow density anomaly at $\rho_i = 0.5$ kg m^3 while keeping all other parameters the same as in model run 2. According to YC97 the scales for the offshore limit for this buoyant discharge are $y_s = 11.5$ km at the surface and $y_b = 9$ km at the bottom. Thus, this plume actually represents the intermediate regime ($0 < y_b < y_s$), but one which is close to a bottom-advected plume (YC97).

The offshore density sections for the two plumes (model runs 2 and 9) at $x = 76.25$ km (i.e., downstream from the source) on day 30 are shown in Figure 16 for the same contour intervals. For model run 2 the flow has strong vertical stratification (isopycnals are almost

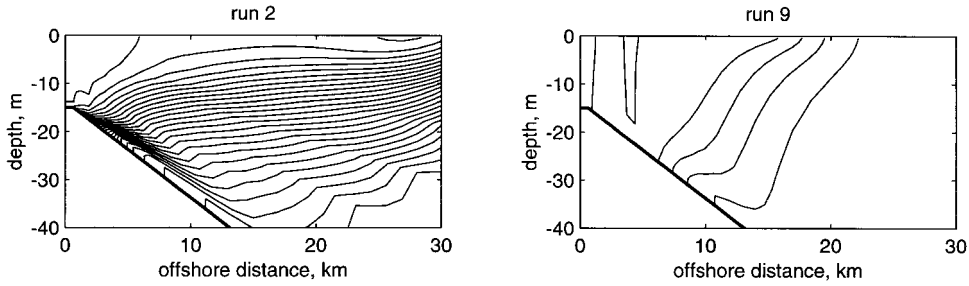

Figure 16. Offshore sections of density anomaly for model run 2 (left panel) and 9 (right panel) on day 20 at $x = 76.25$ km. Contour interval is 0.1 kg m^{-3}.

horizontal), while in model run 9 the buoyant flow inshore is separated from the ambient water offshore by a tilted frontal structure. Sloping isopycnals together with substantially lower density contrast between the plume and the ambient flow facilitate vertical mixing in the case of the bottom-advected plume.

The upstream excursion of buoyant discharge at the surface develops at the beginning of the model run in the same manner as in the previous cases. The upstream and landward counter-current near the bottom is blocked by the imposed boundary conditions for the inflow. This causes the formation of cyclonic vorticity and the upstream turning of the buoyant water in the surface layer. The upstream part of the anticyclonic bulge has a similar structure compared to the previous model runs. This is evident in Figure 17 showing the results of this numerical experiment on day 30. Both streamfunction and density fields indicate the upstream propagation of the plume. As in model run 5, the upstream bulge has substantially lighter water inshore and upstream from the center of the anticyclonic turning (in the sense of streamfunction). The density distribution at the bottom shows that offshore advection of buoyant water in the bottom Ekman layer occurs only downstream from the source (Fig. 17, bottom panel) where the water with the inflow density anomaly is present. This water extends offshore along the bottom over the distance of 9–10 km at its maximum which is in agreement with the y_b estimation. Upstream from the inflow, the water spreads in the manner of surface-advected plume. Indeed, the density anomaly upstream from the source at the bottom is much weaker and occupies less area than at the surface (Fig. 17) because the upstream flow sets the bottom Ekman transport toward the coast. Thus, the mechanism for the upstream spreading of buoyant water is identical for two distinctive types of plumes.

4. Discussion

In the introduction we listed some modeling papers where the upstream spreading of buoyant discharge had been reported. It is instructive to compare those and some other results against the mechanism for upstream spreading which we proposed in the previous section. We will start with the studies where SPEM was utilized. Chapman and Lentz

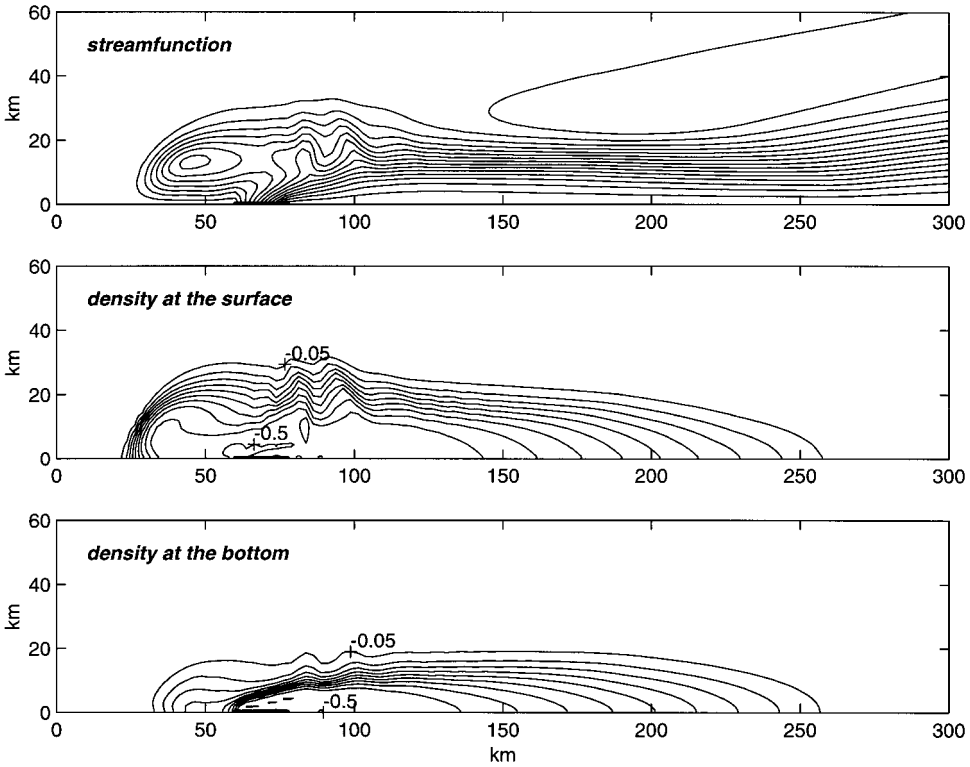

Figure 17. Model run 9, day 30. Plan views of the streamfunction (top panel), density anomaly at the surface (middle panel) and at the bottom (bottom panel) with the contour interval at 0.05 kg m^{-3}.

(1994) described the physics of bottom-advected plumes. Their model geometry and boundary conditions were similar to this study (our model run 9 is the most relevant) and the upstream spreading was repeatedly observed, except in the case when the inflow did not have a density anomaly, as in model run 1 here. They also showed that even weak background downstream flow could arrest the upstream propagation. YC97 and Narayanan (1999) specified uniform downstream flow through the model domain in order to prevent upstream spreading in their numerical experiments. Fong (1998) used a different primitive equation model (ECOM-3D) but he applied the same boundary conditions for buoyant discharge. The upstream spreading of the surface-advected plume occurred in several of his model runs. Garvine (1999) specified both inflow and outflow through the coastal wall of the same net transport but these currents were constant and depth-independent, thus they did not include baroclinic structure of the inflow. The upstream spreading in this study was significant and it also depended on the effect of rotation (i.e., on the Kelvin number of buoyancy source) clearly showing the geostrophic nature of the upstream flow.

Our results presented in Section 3 show that the boundary conditions for buoyant discharge, as in the previous examples (i.e., fixed uniform inflow through the coastal gap),

are responsible for the generation of cyclonic vorticity at the upstream edge of the inflow. This vorticity disturbance causes the initial upstream excursion of buoyant flow which in turn initiates the upstream spreading. We introduce a modified boundary condition (3.1) for buoyant inflow. It maintains the same vertically integrated buoyant inflow at every grid point but allows vertical structure of the offshore velocity at the mouth that is adjusted to the interior dynamics. This boundary condition reduces the upstream excursion especially at the earlier stage of plume's formation (through day 10). Also, the resulting anticyclonic bulge is shifted downstream compared to the standard case.

There are model studies which utilize somewhat different boundary conditions for the inflow, but if the countercurrent in the lower layer is blocked by the superimposed boundary conditions or estuary geometry, the upstream (cyclonic) turning of buoyant inflow still results. For example, Kourafalou *et al.* (1996) specified a fresh water source through the continuity equation. The river discharge was modeled as a volume flux of zero salinity water in one or several coastal nodes of the top layer. They introduced a river channel in model geometry, but it was only 20 km long (4 grid points); thus, it could not prevent the blockage of the countercurrent in the estuary. Most of their process studies' runs revealed the upstream spreading of buoyant discharge. Similar boundary conditions were applied at the coastal wall by Xing and Davies (1999) and their buoyant plume spread some distance upstream over 20 days. Chao and Boicourt (1986) included an estuary with two-layer inflow/outflow boundary condition at its head. They found upstream spreading in only one model run with no bottom friction. In that numerical experiment, the landward flow near the bottom ran into the estuary at unrealistically high speed and was ultimately blocked at the estuary head. This in turn induced cyclonic vorticity and convergence in the estuary's lower layer with corresponding upstream excursion of buoyant inflow at the surface. Garvine (2000) conducted a series of model experiments with different types of boundary conditions at the mouth and found that more realistic and sophisticated conditions tend to reduce the upstream penetration. He also found that lower vertical mixing diminished the upstream spreading and, in general, the growth of the anticyclonic bulge.

In other studies the model geometry was configured in such a way that the baroclinic flow in the lower layer passed into the mouth unobstructed. Oey and Mellor (1993) applied an elaborate storage basin in their model domain to provide a sink for the landward flow in the lower layer through the mouth. As a result, the buoyant flow from the estuary propagated directly into the coastal ocean without cyclonic deviation at the mouth during the earlier stage of their calculations (day 11). This pattern is similar to our results with boundary condition (3.1). Later in time (day 40) their bulge grew and a surface salinity minimum was clearly formed in the upstream-nearshore segment of the anticyclone (as in our run 5). At this stage buoyant inflow advanced some 40 km upstream and this tendency seemed to continue on day 47 (the last available figure in their paper).

Masson and Cummins (1999) conducted numerical simulations of a buoyancy driven current around Vancouver Island. Their model well resolved the dynamics through the mouth (Juan de Fuca Strait). Their numerical experiments with buoyant forcing only

continued for more than 200 days but did not exhibit the upstream spreading of buoyancy either for constant runoff (the mean annual Fraser River discharge) or for the high runoff corresponding to the summer freshet period. However, this might be in part due to the topographic steering of buoyant inflow, since Juan de Fuca Strait tilts significantly downstream. Results of Garvine (2000) also demonstrated the importance of spatial orientation of the estuary axis, i.e., direction of the discharge relative to the coastline.

The observations presented by Beardsley *et al.* (1985) suggest that the Changjiang discharge turned to the left during high runoff (in summer). These observations fit our proposed explanation. First, the countercurrent near the bottom along the offshore flank of the buoyant plume was in part blocked by the topographic step-like feature at the mouth. Second, the Changjiang discharge during high runoff should form a surface-advected plume with substantial offshore expansion because of the large density difference between the plume and the ambient waters (>5 kg m^{-3}) as well as due to the high net transport. For the surface advected plumes, buoyant water in the anticyclonic bulge spreads offshore over at least four baroclinic Rossby radii (YC97). Furthermore, tidal mixing was also strong (tidal velocities reached 1.5 m s^{-1}) favoring high vertical diffusion. This could produce substantial density difference within the anticyclonic bulge. The surface salinity maps during the high runoff showed a massive expansion of low saline waters upstream and offshore over a distance of more than 100 km with the tongue of less saline water nearshore and upstream from the mouth. Numerical experiments on the formation of Changjiang River plume (Bang and Lie, 1999) with realistic topography and under conditions of high runoff showed that strong upstream penetration occurred both with and without wind forcing (no matter what the direction of wind stress was, provided the wind forcing was not overwhelmingly strong).

Weingartner *et al.* (1999) presented evidence for significant upstream spreading of buoyant discharge of the major Siberian rivers in the Arctic. Similarly, a thermal IR image of the Mackenzie shelf region in the Beaufort Sea provided by K. Engle and T. Weingartner (Geophys. Res. Let., 1999, 26, No 15, cover) showed upstream propagation of the Mackenzie River plume. However, in both cases the authors attributed upstream winds as a possible reason for the upstream spreading. Thus, the role of the intrinsic plume dynamics in these events is ambiguous and requires further investigation.

5. Summary

In this study we have addressed the problem of the upstream spreading of buoyant inflow into the coastal ocean. This appears to be a common feature in numerical models of buoyant coastal plumes. On the other hand the observational evidence for this phenomena is rare. The generation of upstream buoyant flow in model studies is caused by the following processes:

(1) In many cases boundary conditions oversimplify the dynamics at the mouth. The naturally developing countercurrent in the lower layer (resulting from the baroclinic adjustment of the discharge) tends to flow landward through the mouth but often is blocked by the superimposed fixed inflow specified as a boundary condition. This blockage results

in the generation of a strong cyclonic vorticity disturbance with corresponding convergence at the bottom and divergence at the surface. As a result of surface divergence the buoyant flow first deviates upstream from its source and only after that turns anticyclonicly to form a buoyant current propagating downstream along the coast.

(2) However, the initial upstream excursion of the inflow at the source does not guarantee predominantly upstream spreading of the anticyclonic bulge. In fact, this bulge can grow symmetrically (i.e., in all directions) from the source. Vertical mixing causes the enhanced upstream propagation of the anticyclonic bulge. While circulating around the center of the anticyclone, the fresher water gradually becomes saltier due to vertical mixing and diffusion. As a result, the pool of lightest water does not coincide with the center of the anticyclone (in the sense of the integral streamfunction) but tends to occupy the upstream and inshore segment of the bulge where the buoyant water comes first. This sets a new center for the anticyclonic turning at the surface and promotes the upstream shift of the anticyclonic bulge. Interestingly, a similar tendency is well known in meteorology: when the center of pressure and the center of warm air at high altitude in an anticyclone do not coincide, the anticyclone will shift with height toward the center of the warm air (Gill, 1982).

However, the upstream spreading of buoyant coastal discharge is still possible and has been observed in nature. These dynamics most likely can be observed when the discharge has strong density anomaly and great net transport. This will enable the formation of a surface-advected plume with significant offshore expansion of the anticyclonic bulge over a rather short period of time (say between two consecutive wind events). All examples from the previous section, i.e., the Changjiang, the Mackenzie and the Siberian rivers' plumes under high runoff conditions fall in this category. Of course upwelling-favorable wind can also contribute to the upstream propagation of a buoyant plume. However, it is likely that the intrinsic dynamics of the plume is the major cause. In fact, upwelling favorable wind can further amplify this process producing greater offshore expansion and additional vertical mixing of buoyant water. In contrast to the largest plumes referred above, the medium-size plumes like the Delaware Coastal Current (Münchow and Garvine, 1993), the Chesapeake plume (Boicourt, 1973) or the Columbia River plume in winter season (Hickey *et al.,* 1998) do not exhibit upstream spreading even under the upwelling favorable wind events of limited duration.

Acknowledgments. Financial support was provided by the National Science Foundation Grant OCE-9907995. I would like to thank Rich Garvine, Dave Chapman, Bob Beardsley and Barry Klinger for their insightful comments and suggestions. I am also indebted to Chandra Narayanan for his assistance with the installation of SPEM5.1.

REFERENCES

Bang, I. and H.-J. Lie. 1999. A numerical experiment on the dispersion of the Changjiang River plume. J. Korean Soc. Oceanogr., *34,* 185–199.

Beardsley, R. C. and J. Hart. 1978. A simple theoretical model for the flow of an estuary onto a continental shelf. J. Geophys. Res., *83,* 873–883.

Beardsley, R. C., R. Limeburner, H. Yu and G. A. Cannon. 1985. Discharge of the Changjiang (Yangtze River) into the East China Sea. Continental Shelf Res., *4,* 57–76.

Boicourt, W. C. 1973. The circulation of water on the continental shelf from Chesapeake Bay to Cape Hatteras. Ph.D. dissertation, The Johns Hopkins Univ., 183 pp.

Chao, S.-Y. and W. C. Boicourt. 1986. Onset of estuarine plume. J. Phys. Oceanogr., *16,* 2137–2149.

Chapman, D. C. and S. J. Lentz. 1994. Trapping of coastal density front by the bottom boundary layer. J. Phys. Oceanogr., *24,* 1464–1479.

Csanady, G. T. 1978. The arrested topographic wave. J. Phys. Oceanogr., *8,* 47–62.

Fong, D. A. 1998. Dynamics of freshwater plumes: observations and numerical modeling of the wind-forced response and alongshore freshwater transport. Ph.D. dissertation, MIT-WHOI, 172 pp.

Garvine, R. W. 1995. A dynamical system for classifying buoyant coastal discharge. Continental Shelf Res., *15,* 1585–1596.

—— 1999. Penetration of buoyant coastal discharge onto the continental shelf. J. Phys. Oceanogr., *29,* 1892–1909.

—— 2000. The impact of prescribed inlet flow fields on buoyant coastal discharge. J. Mar. Res., Artifacts in buoyant coastal discharge models: An observational and model study.

Gill, A. E. 1982. Atmosphere-Ocean Dynamics, Academic Press, 662 pp.

Haidvogel, D. B., J. L. Wilkin and R. Young. 1991. A semi-spectral primitive equation ocean circulation model using vertical sigma and orthogonal curvilinear horizontal coordinates. J. Comput. Phys., *94,* 151–185.

Hickey, B. M., L. J. Pietrafesa, D. A. Jay and W. C. Boicourt. 1998. The Columbia River Plume Study: Subtidal variability in the velocity and salinity fields. J. Geophys. Res., *103,* 10,339–10,368.

Kourafalou, V. H., L.-Y. Oey, J. D. Wang and T. N. Lee. 1996. The fate of river discharge on the continental shelf 1. Modeling the river plume and inner shelf coastal current. J. Geophys. Res., *101,* 3415–3434.

Kubokawa, A. 1991. On the behavior of outflows with low potential vorticity from a sea strait. Tellus, *43A,* 168–176.

Masson, D. and P. Cummins. 1999. Numerical simulation of a buoyancy-driven coastal counter-current off Vancouver Island. J. Phys. Oceanogr., *29,* 418–435.

McCreary, J. P., S. Zhang and S. R. Shetye. 1997. Coastal circulation driven by river outflow in a variable-density 1½-layer model. J. Geophys. Res., *102,* 15,535–15,554.

Mellor, G. L. and T. Yamada. 1974. A hierarchy of turbulence closure models for planetary boundary layers. J. Atmos. Sci., *31,* 1791–1806.

Münchow, A. and R. W. Garvine. 1993. Buoyancy and wind forcing of a coastal current. J. Mar. Res., *51,* 293–322.

Narayanan, C. 1999. Offshore spreading of a buoyant coastal discharge. Ph.D. dissertation, Univ. of Delaware, 267 pp.

Oey, L.-Y. and G. L. Mellor. 1993. Subtidal variability of estuarine outflow, plume, and coastal current: A model study. J. Phys. Oceanogr., *23,* 164–171.

Pichevin, T. and D. Nof. 1997. The momentum imbalance paradox. Tellus, *49A,* 298–319.

Weingartner, T. J., S. Danielson, Y. Sasaki, V. Pavlov and M. Kulakov. 1999. The Siberian Coastal Current: A wind and buoyancy-forced Arctic coastal current. J. Geophys. Res., *104,* 29,697–29,713.

Woods, A. W. and R. C. Beardsley. 1988. On the barotropic discharge of a homogeneous fluid onto a continental shelf. Continental Shelf Res., *8,* 307–327.

Yankovsky, A. E. and D. C. Chapman. 1997. A simple theory for the fate of buoyant coastal discharges. J. Phys. Oceanogr., *27,* 1386–1401.

Xing, J. and A. M. Davies. 1999. The effect of wind direction and mixing upon the spreading of a buoyant plume in a non-tidal regime. Continental Shelf Res., *19,* 1437–1483.

Received *8 November, 1999;* revised: *6 April, 2000.*